PIER M

A Metamaterial Based Dual-Band UWB Antenna Design for 5G Applications

Jincheng Xue, Guolong Wang, Shuman Li, Zhuopeng Wang, and Quanquan Liang*

Electronic and Information Engineering, Shandong University of Science and Technology, Qingdao, China

ABSTRACT: This paper presents the design of a novel ultra-wideband antenna for Internet of Things applications utilizing metamaterials. The antenna is fed by a coplanar waveguide and comprises several key components: two relatively connected co-directional split-ring resonators with an upper feeder, a ground plane featuring a complementary circular resonant slit, and a double C-shaped nested ring situated on the lower surface of the substrate constitutes the electric inductive capacitive (ELC) element. The antenna's overall dimensions are $0.408 \times 0.35 \times 0.018 \lambda_0^3$, enabling it to operate within the dual-band frequencies of 2.79–4.22 GHz (40.8%) and 4.70–5.88 GHz (22.3%). The antenna exhibits a favorable directional pattern across its operating frequency range, with a measured peak gain of approximately 3.93 dBi. This performance makes it suitable for applications in Wi-Fi, 5G communication, IoT, and various other fields requiring reliable wireless connectivity.

1. INTRODUCTION

The continuous advancement of 5G communication technology has led to the introduction of a new air interface called 5G New Radio (5G NR). This air interface is designed specifically to meet the requirements of future 5G operations, providing enhanced communication link technology between mobile devices and base stations within cellular networks. The Third Generation Partnership Program recently released and approved new spectrum for future 5G NR networks [1]. Given the limited spectrum resources in 5G multi-band communications, recently there has been discussion regarding the allocation of unlicensed LTE band 46 (5.15–5.925 GHz). This paper aims to design a dual-band ultra-wideband antenna utilizing metamaterials, with the objective of covering a broad range of frequency band applications mentioned above.

As the communication industry continues to advance, there is a growing demand for increased channel capacity and higher-speed transmission efficiency. Consequently, the frequency spectrum of 5G NR communication systems is being extensively developed and applied. In [2–7], researchers employed various antenna designs to fulfill the requirements of specific design frequency bands. In [2], a compact broadband antenna featuring a wide side and conical diversity pattern, tailored for 5G NR applications, is proposed. This antenna is constructed using parallel coupled lines of a quarter wavelength and blocky LC elements, achieving an impedance bandwidth of 3.16–3.81 GHz. In [4], a multiple-input multiple-output (MIMO) antenna array is created by incorporating eight identical antennas into a metal frame. Each antenna consists of an L-shaped slit and a microstrip feeder, effectively covering the

n77, n78, n79, and WLAN 5G bands within the 5G NR spectrum, while maintaining high isolation.

Metamaterials, owing to their distinctive properties, find extensive application in antenna design for purposes such as reducing radar cross-section, enhancing bandwidth and gain, and altering polarization characteristics. In [8, 9], a zero-refractive index metamaterial design was introduced to enhance antenna gain [8]. This involved proposing a metamaterial lens which, in conjunction with an artificial magnetic conductor (AMC), cooperated to boost antenna gain [9]. Additionally, a metamaterial periodic array was utilized to enhance gain and achieve circular polarization. In [10], a three-layer ring metamaterial absorber configuration was proposed, yielding a double-ring structure with optimal electromagnetic wave absorption properties. This effectively reduced the radar cross-section (RCS) of the antenna without compromising its radiation performance. In [11, 12], metamaterials were employed to transition traditional microstrip antennas from linear to circular polarization, facilitating polarization conversion. The miniaturization of dual-band antennas was achieved through the adoption of U-shaped and inverted U-shaped structures on a double-layer substrate [13].

In this paper, a novel metamaterial is devised, featuring two relatively connected co-directional split-ring resonators. Subsequently, a new metamaterial structure is established by incorporating a double C-shaped nested ring on the lower surface which constitutes the ELC element. The antenna's primary structure comprises metamaterial elements along with microstrip feeders. To attain a satisfactory match within the 5G frequency band, circular complementary slots are introduced on the ground plane. The antenna design encompasses both 5G New Radio (NR) and Wi-Fi frequency bands.

* Corresponding author: Quanquan Liang (quanquan_sdust@sdust.edu.cn).

85

2. LEFT-HANDED STRUCTURE DESIGN

In this paper, a novel metamaterial, denoted as Metamaterial I, is introduced. The structure is shown in Figure 1. It is constructed by printing two relatively connected co-directional split-ring resonators of distinct sizes on the surface and connected by a microstrip line. Upon vertically incident electromagnetic waves, the reflection coefficient is depicted in Figure 2. The metamaterial exhibits a minimum reflection coefficient around 2.5 GHz and 3 GHz, accompanied by phase variations at these frequencies.
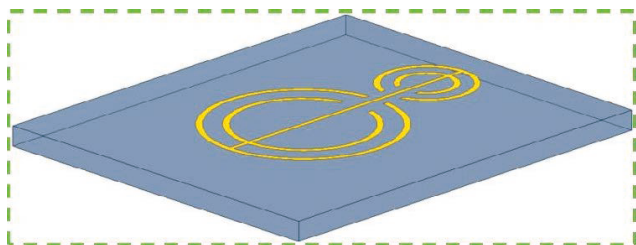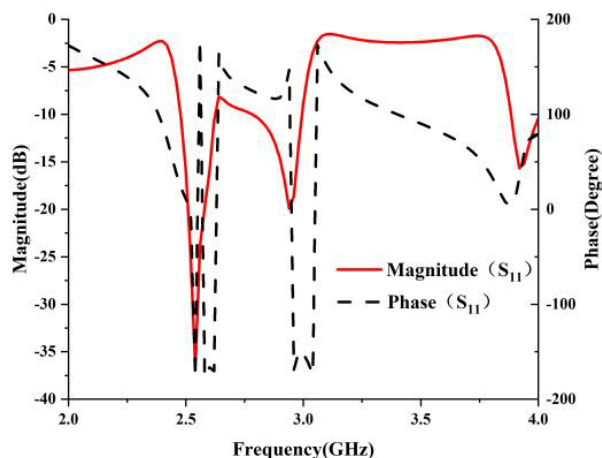

FIGURE 1. Metamaterial I.

FIGURE 2. Amplitude and phase of the metamaterial reflection coefficient.

The process involved in the equivalent circuit analysis of left-hand Metamaterial I is comprehensive. Upon the incidence of an electromagnetic wave, the entire structure induces current, leading to the introduction of inductance into both the connecting line and a single opening ring in the same direction. Additionally, coupling capacitance arises within the gap of the opening ring, between the opening ring and the connecting line, and within the opening ring itself. This analysis results in the creation of the equivalent circuit diagram, as depicted in Figure 3.

To determine the parameter values of its components, we employed Advanced Design System (ADS) for simulation and optimization. Specifically, inductors L_1–L_4 correspond to the inductance introduced by the lower end of the same open crack ring, while L_5–L_8 represent the inductance introduced by the upper end of the small open crack ring. L_9 denotes the induc-
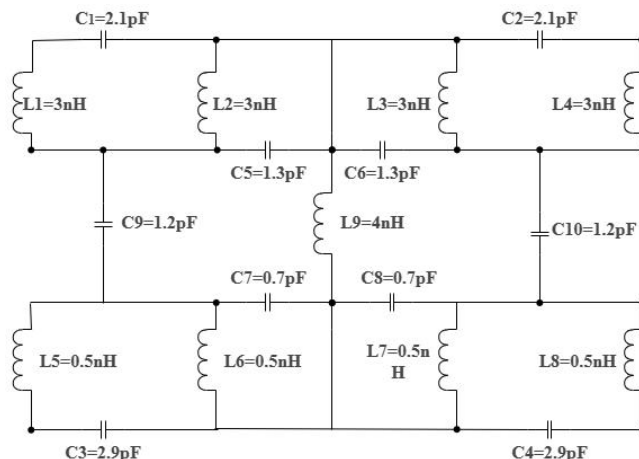

FIGURE 3. Equivalent circuit model.

tance introduced by the connecting line. On the other hand, the resonant capacitance C_1–C_4 emerges between the same direction slit rings, while the coupling capacitance C_5–C_8 forms between the gap of the open ring and the connecting line. Furthermore, C_9 and C_{10} represent the coupling capacitance generated between the upper and lower two same direction slit rings.

Figure 4 presents the reflection coefficient and phase simulated by the equivalent circuit diagram in ADS. The results indicate that the equivalent circuit model exhibits the lowest reflection coefficient and significant phase changes around 2.5 GHz and 3 GHz, consistent with the simulation results of the left-handed structure. Hence, we assert the correctness of the equivalent circuit model.

Subsequently, the equivalent permittivity and permeability of the structure are determined using a parameter inversion method. Initially, the S-parameters of Metamaterial I are acquired using electromagnetic simulation software. Subsequently, the equivalent permittivity and permeability can be approximated utilizing the following formula [14]:

$$\varepsilon = \frac{n_e}{z} \tag{1}$$
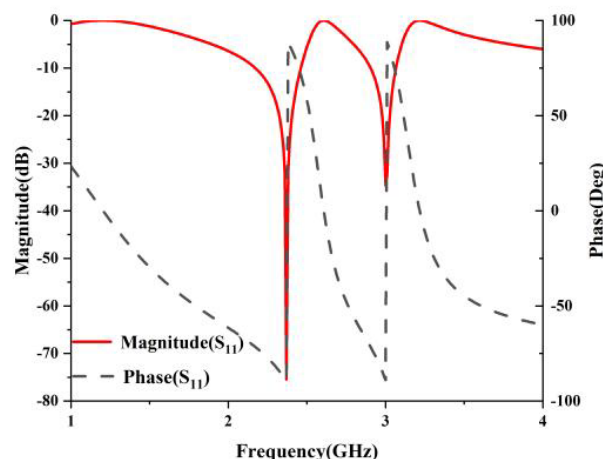
$$\mu = n_e z \tag{2}$$

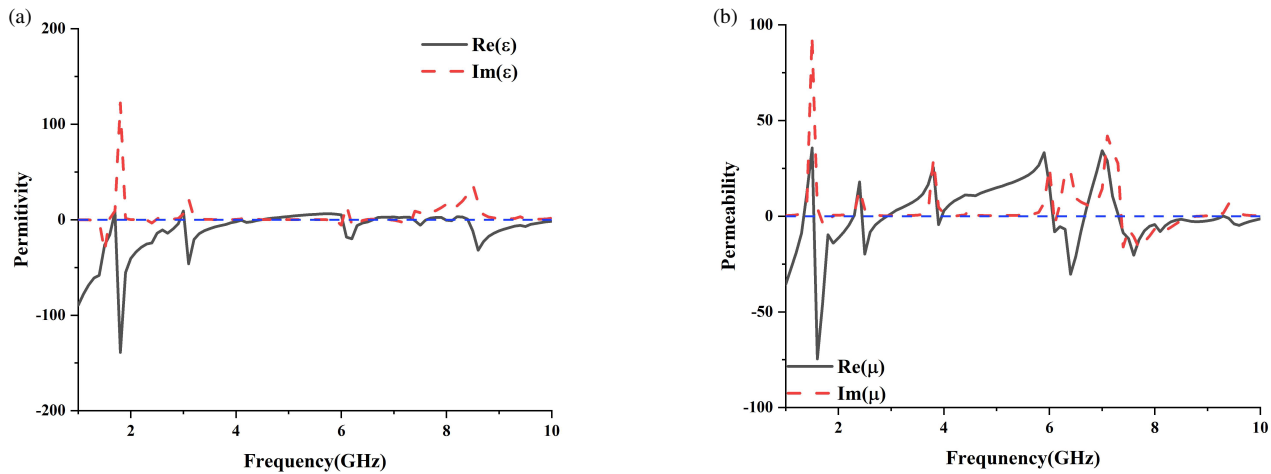FIGURE 4. The reflection amplitude and phase of the equivalent circuit.

FIGURE 5. Equivalent permittivity and permeability of Metamaterial I.

In the formula:

$$n_e = \frac{1}{kh} \cos^{-1}\left[\frac{1 - S_{11}^2 + S_{21}^2}{2S_{21}} + \frac{2\pi\mu}{kd}\right] \qquad (3)$$

$$z = \pm\sqrt{\frac{(1 + S_{11})^2 - S_{21}^2}{(1 - S_{11})^2 - S_{21}^2}} \qquad (4)$$

where ε is the effective dielectric constant; n_e is the effective refractive index; z is the wave impedance; μ is the effective permeability; k is the wave number; h is the thickness of meta-material; S_{11} and S_{21} are scattering parameters. u is an integer that represents the branch of the inverse cosine function.

Figure 5 illustrates the equivalent permittivity and permeability obtained through S-parameter inversion of the relatively connected co-directional split-ring resonators. The real part of the equivalent permittivity for Metamaterial I exhibits negativity within the frequency ranges of 1.9–2.9 GHz and 3.1–4.4 GHz, while the real part of the equivalent permeability demonstrates negativity specifically within the 2.6–2.9 GHz band. In the configuration of the open ring, current flows along the surface ring, establishing a circular current path. This circulating current generates a magnetic field that surrounds the open ring. The orientation of this magnetic field is perpendicular to the direction of the electric field, adhering to the principles of the left-hand coordinate system. By designing a relatively co-directional split-ring structure, the inductance and capacitance within the system are altered. This modification effectively introduces an inductor during the connection process. Consequently, the structure exhibits characteristics of negative permeability and negative dielectric constant within the specified frequency range.

Building upon the foundation of Metamaterial I, a novel Metamaterial II is created by overlaying double C-shaped nested rings onto the lower surface of the dielectric substrate that constitutes the ELC element. Figure 6 shows the structure of Metamaterial II, while Figure 7 depicts its corresponding equivalent permittivity and permeability. The real part of the
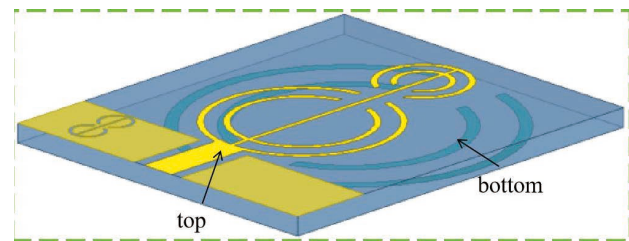

FIGURE 6. Metamaterial II.

equivalent permittivity for Metamaterial Structure II exhibits negativity within the frequency bands of 2.39–3.61 GHz and 3.69–6.1 GHz. Similarly, the real part of the equivalent permeability demonstrates negativity within the frequency ranges of 2.39–2.65 GHz and 4.87–5.877 GHz. The left-handed Metamaterial Structure II exhibits double negative characteristics within the frequency ranges of 2.39–2.65 GHz and 4.87–5.87 GHz. Compared with Metamaterial I, Metamaterial II has a wider double negative characteristic bandwidth.

3. ANTENNA DESIGN

This paper introduces a dual-band ultra-wideband antenna loaded with metamaterials, as depicted in Figure 8. The antenna is fabricated on an FR-4 dielectric substrate measuring 1.6 mm in thickness. The upper-end radiator of the antenna consists of two co-directional split-ring resonators with a line width of 0.5 mm and a connecting line, incorporating open rings of varying sizes to achieve dual-frequency operation. The antenna is fed using a coplanar waveguide. The optimized geometric parameters are presented in Table 1.

The design evolution of the dual-frequency ultra-wideband antenna based on metamaterials, as depicted in Figure 9, and the impedance bandwidth and gain changes of the antenna are shown in Figure 10. Initially, the antenna, referred to as Antenna A, operates at dual frequencies, 3.7 GHz and 4.9 GHz, with a limited left-hand characteristic bandwidth. To address this limitation, Antenna B is devised by introducing a single-loop complementary slot on the ground. This alteration influ-
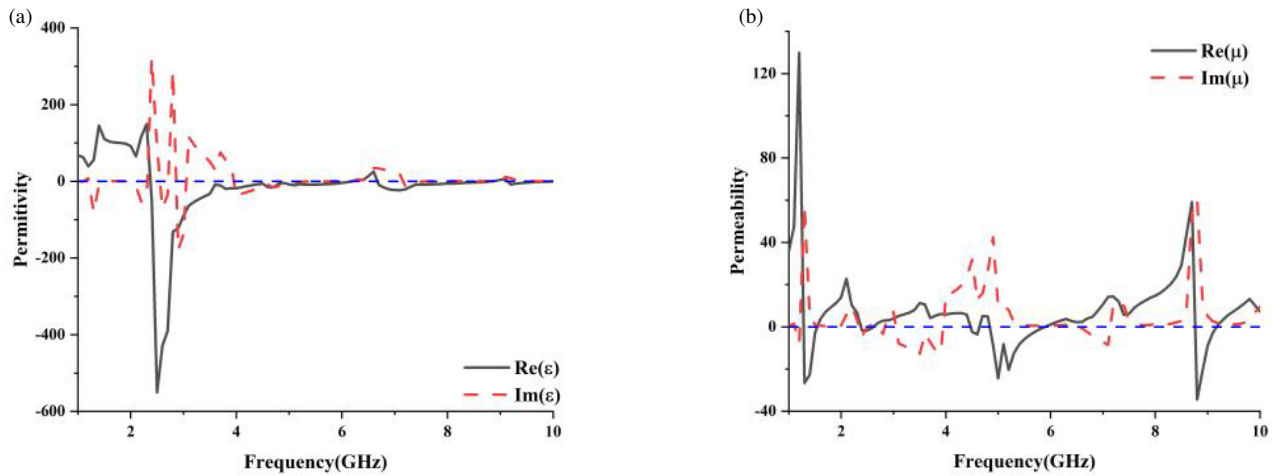
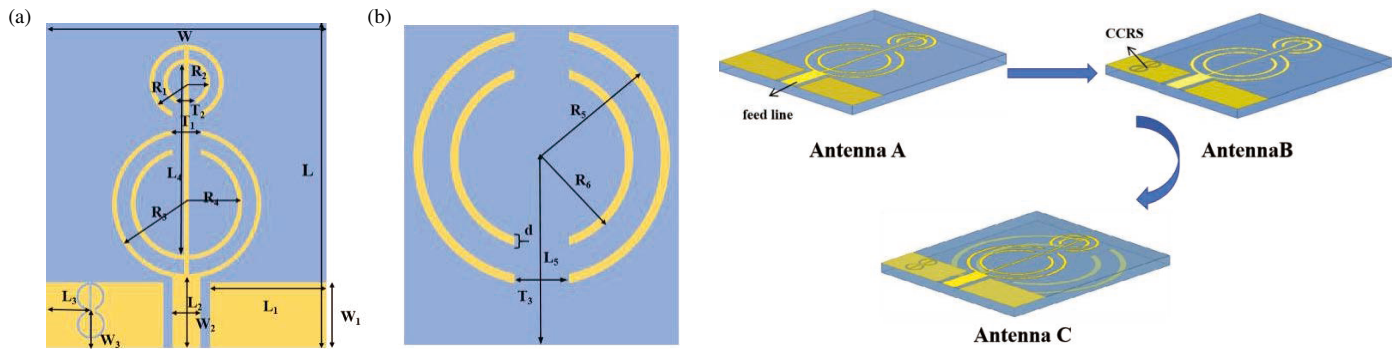FIGURE 7. Equivalent permittivity and permeability of Metamaterial II.

FIGURE 8. Antenna structure diagram. (a) Top view. (b) Bottom view.

FIGURE 9. Antenna design process.

TABLE 1. Antenna size parameters.

Parameters	Unit/mm	Parameters	Unit/mm	Parameters	Unit/mm
W	30	W_1	7.1	R_1	4
L	35	W_2	3	R_2	2.5
L_1	12.5	W_3	4	R_3	8
L_2	7.64	d	1	R_4	6
L_3	5	T_1	3	R_5	14
L_4	20.5	T_2	2	R_6	10
L_5	20.5	T_3	6.2		

ences the current distribution on the ground, thereby modifying the transmission line's characteristics and the current distribution of the antenna radiator. Consequently, the antenna's performance in the 5G frequency band is enhanced, leading to increased bandwidth and improved matching. Building upon Antenna B, Antenna C incorporates a double C-type nested ring on the lower surface of the dielectric substrate. This addition introduces a new left-handed structure, resulting in expanded overall left-handed characteristic bandwidth, enhanced resonant coupling, and significantly increased bandwidth at the low-frequency band. Compared to Antenna A, the final design, Antenna C, achieves substantial improvements. The antenna finally achieves dual-band UWB of 2.79–4.22 GHz and 4.70–5.88 GHz. Compared with Antenna A, the final antenna achieves 28.5% increase in impedance bandwidth and 6.2% miniaturization at low frequency. The impedance matching at the high frequency is better; the relative bandwidth is increased by 5%; the dual-band gain is increased; and the peak gain is about 3.9 dBi.
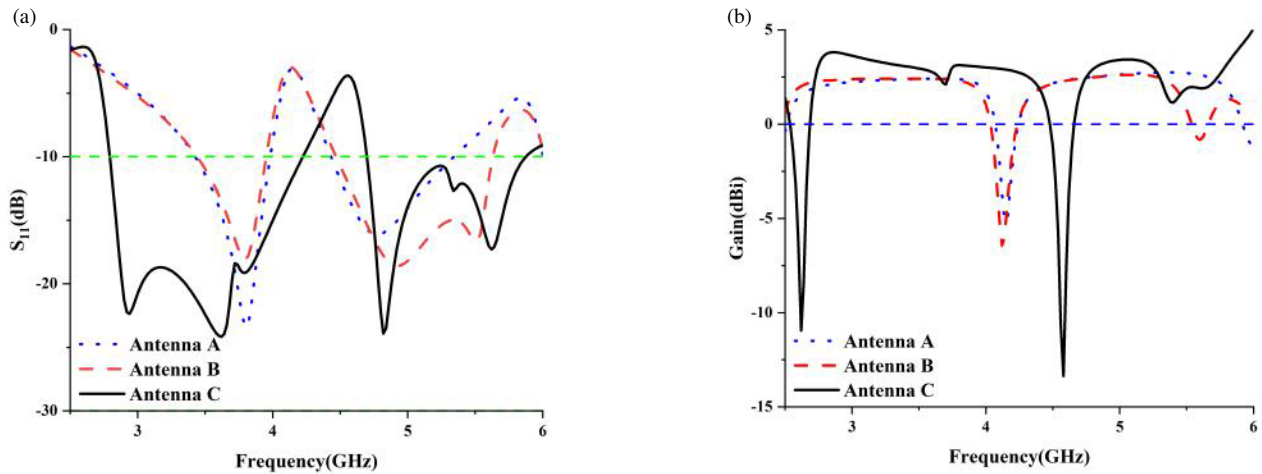
FIGURE 10. Simulation variations of the three antennas. (a) S_{11}. (b) Gain.
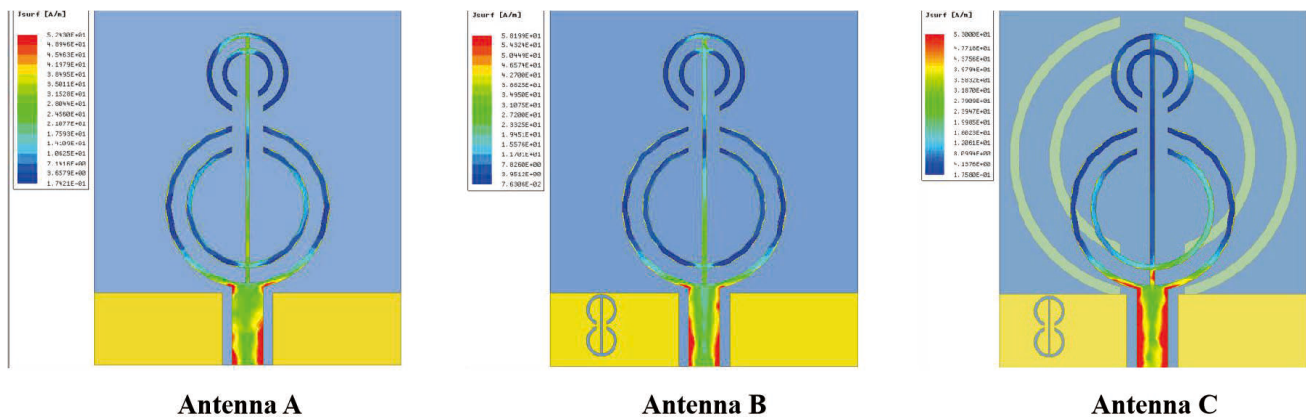

FIGURE 11. Current change of the antenna at 3.6 GHz.

The current variation at 3.6 GHz during the antenna design process is shown in Figure 11, providing insights into the changes in the antenna's operating bandwidth. Analyzing Figure 10, it is apparent that the introduction of the ground slot, from Antenna A to antenna B, has a minimal impact on the current distribution on the surface of the antenna radiating body at 3.6 GHz. Consequently, the bandwidth of the antenna in the lower frequency band remains relatively stable. Subsequently, with the superposition of the same-direction opening ring on the lower surface, there is a notable increase in the current on the antenna radiator, particularly at the larger opening ring on the upper surface. This substantial current enhancement contributes to the observed increase in the bandwidth of Antenna C within the lower frequency band.

The current variation at 5 GHz during the antenna design process is shown in Figure 12. Upon opening the circular complementary resonant slot on the ground, a discernible effect is observed on the current distribution, particularly at the smaller open ring located at the upper end. The current at this smaller open ring is amplified, elucidating how the ground slot enhances the impedance matching of the antenna at the higher frequency band. Subsequently, upon loading the lower surface open ring, although the current distribution remains relatively

unchanged, there is a obvious increase in current magnitude. This enhancement in current magnitude contributes to achieving superior impedance matching in the higher frequency band of Antenna C.

4. PARAMETRIC RESEARCH

Analyzing the parameter T_1, which denotes the size of the opening ring on the antenna radiator, within the range of 1 mm to 4 mm, reveals a significant impact on the equivalent electromagnetic parameters of Metamaterial II. As T_1 varies, both the antenna bandwidth and resonant frequency undergo changes, consequently influencing the antenna's overall performance. Figure 13 illustrates the simulation curve of the S_{11} parameter as T_1 varies. Through iterative simulations, the optimal opening size T_1 for the antenna radiator's ring is determined to be 3.0 mm.

Figure 14 depicts the simulation curve of S_{11} as the opening size of the codirectional fracture ring on the lower surface of the dielectric substrate, denoted as T_3, varies. The range of T_3 examined spans from 5.4 to 6.2 mm, each resulting in different electromagnetic characteristics for Metamaterial II. These variations directly impact radiation characteristics, such as the an-
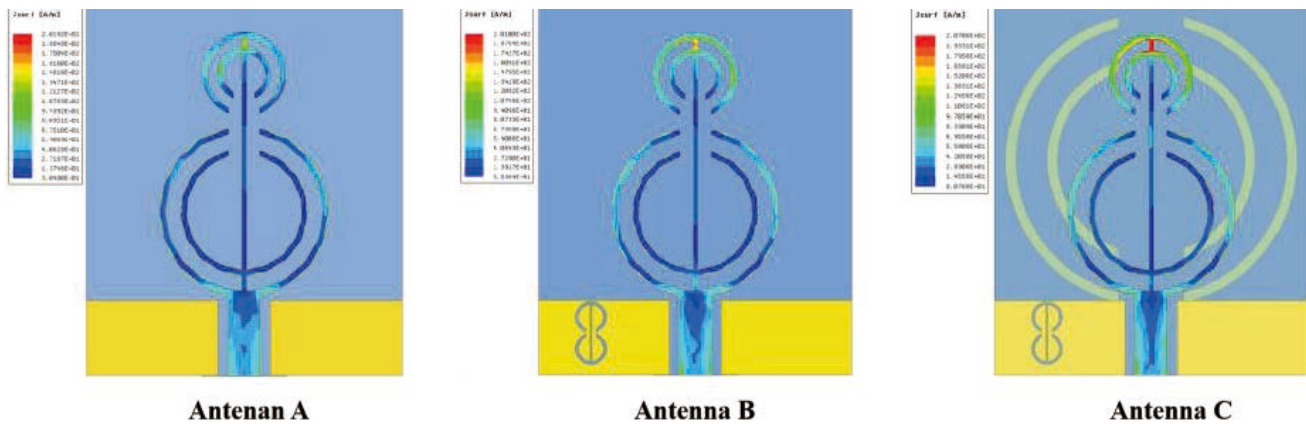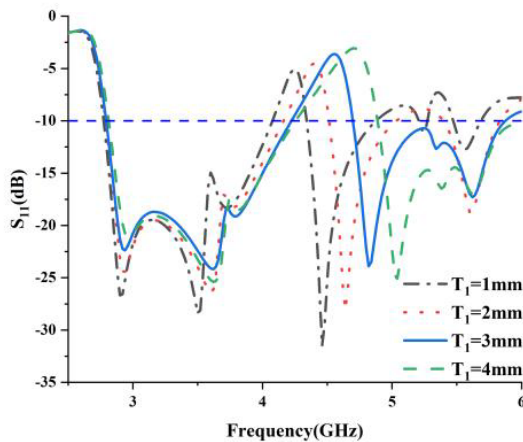
FIGURE 12. Current change of the antenna at 5 GHz.

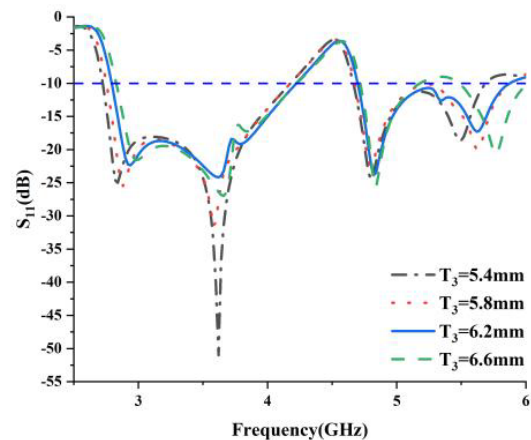FIGURE 13. S_{11} simulation curves for each value of T_1.

FIGURE 14. S_{11} simulation curves for each value of T_3.

tenna's bandwidth, thereby influencing its overall performance. Observing Figure 14, it is noted that as T_3 increases, there is a slight backward shift in the antenna bandwidth. Therefore, after careful consideration, an optimal T_3 value of 6.2 mm is selected to ensure favorable impedance matching and overall antenna performance within the 5G band.

5. SIMULATION AND MEASUREMENT

In Figure 15, a physical image of the antenna is depicted. Moving on to Figure 16(a), a comparison between the simulated and measured S_{11} parameters is presented. The figure demonstrates that while there might be a slight backward shift in the higher frequency band, the overall trend of the measured S_{11} closely aligns with the simulated results. This suggests that the antenna design performs as expected across different frequency bands. Figure 16(b) provides the gain and radiation efficiency. The figure shows that the simulated gain is in good agreement with the measured gain, indicating consistency between simulation and practical performance. Additionally, the radiation efficiency, mostly above 80%, reflects the antenna's effectiveness in radiating electromagnetic energy.

Figure 17 shows the simulated and measured directional patterns of the antenna at 3.5 GHz and 5.0 GHz, which show that the antenna has good omnidirectionality. Table 2 provides a comprehensive comparison of the antenna performance presented in this paper with that of other studies. Upon reviewing Table 2, it becomes evident that the antenna designed in this paper offers several advantages compared to those pre-
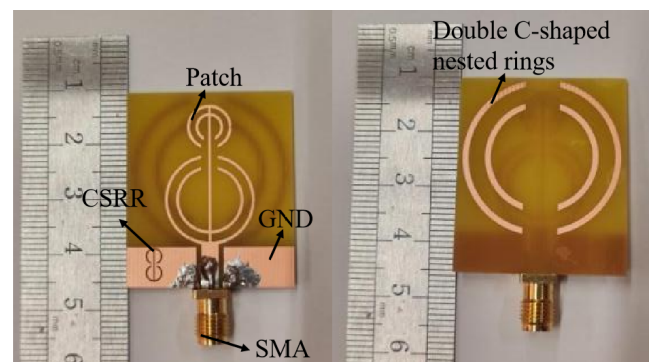

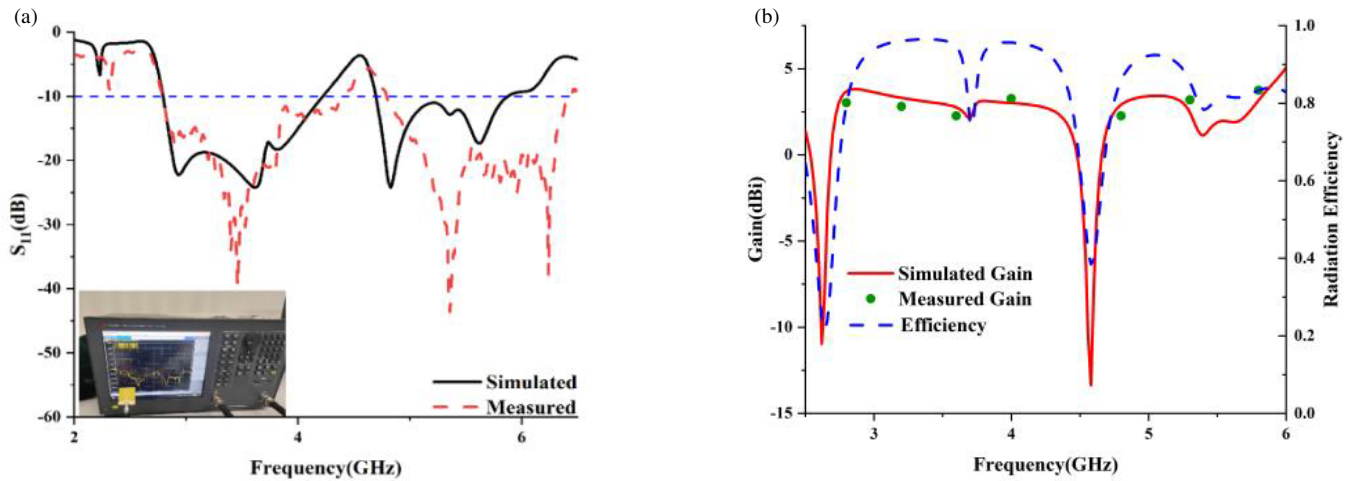
FIGURE 15. Physical antenna diagram.

FIGURE 16. Simulation and measurement results. (a) S_{11}. (b) Gain, efficiency.
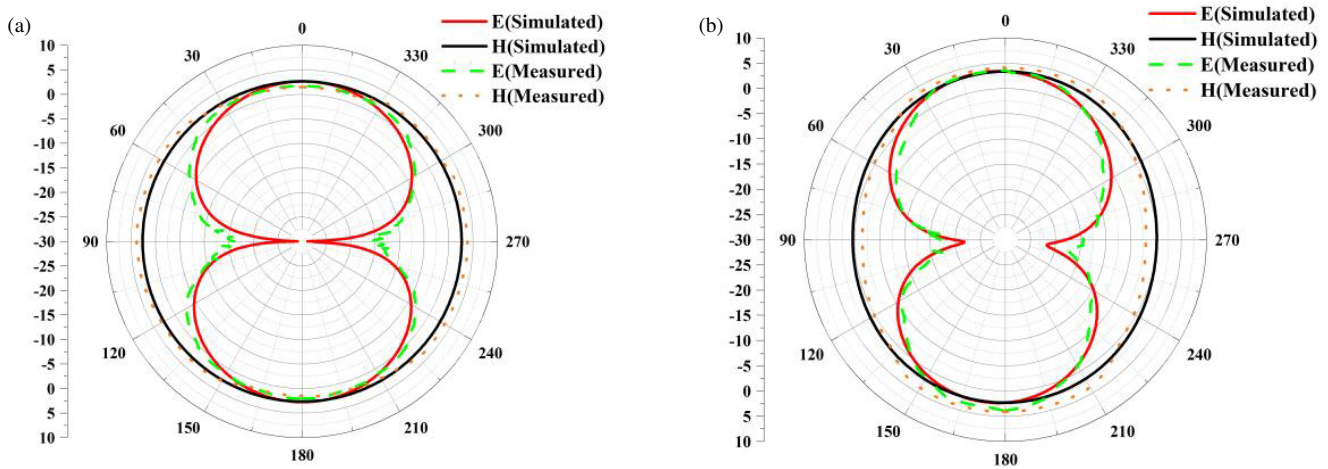

FIGURE 17. Antenna pattern, (a) 3.5 GHz, (b) 5.0 GHz.

TABLE 2. Performance comparison between this design and other antennas.

Reference	Overall dimension (λ_0^3)	Resonance (GHz)	$S_{11} < -10\,\text{dB}$ (GHz)	Gain (dBi)
[15]	$0.511 \times 0.244 \times 0.005$	3.55	3.3–3.8	7.38
[16]	$\pi \times 0.33^2 \times 0.14$	3.55	3.3–3.8	8.2
[17]	$0.257 \times 0.257 \times 0.06$	3.5	3.4–3.6	8.1
[18]	$6.72 \times 0.46 \times 0.01$	6.45	5.18–7.71	2.45
This work	$0.408 \times 0.35 \times 0.018$	3.5/5.3	2.79–4.22/4.70–5.88	3.93

sented in other studies. Firstly, it achieves dual-frequency ultra-wideband operation, implying that it can operate effectively across a broad range of frequencies. Additionally, despite its smaller size, this antenna demonstrates superior gain performance, indicating its ability to efficiently radiate electromagnetic energy.

6. SUMMARY

This paper introduces a novel metamaterial design approach aimed at achieving ultra-wideband characteristics for antennas. The proposed metamaterial configuration involves connecting relatively open fissured resonant rings superimposed with double C-shaped nested rings which constitute the ELC element. Ultimately, the antenna achieves an impressive impedance

bandwidth spanning from 2.79 GHz to 4.22 GHz (40.8%) and from 4.70 GHz to 5.88 GHz (22.3%). The measured peak gain is approximately 3.93 dBi, accompanied by a favorable directional pattern. These performance characteristics make the antenna well suited for applications in 5G NR and WiFi systems.

REFERENCES

[1] Liu, H.-Y., C.-Y.-D. Sim, and C.-J. Huang, "Wideband MIMO antenna array design for future mobile devices operating in the 5G NR frequency bands n77/n78/n79 and LTE band 46," *IEEE Antennas and Wireless Propagation Letters*, Vol. 19, No. 1, 74–78, 2019.

[2] Liu, S., Z. Wang, W. Sun, and Y. Dong, "A compact wideband pattern diversity antenna for 5G-NR applications," *IEEE Antennas and Wireless Propagation Letters*, Vol. 21, No. 9, 1787–1791, 2022.

[3] Xu, H., H. Wang, S. Gao, H. Zhou, Y. Huang, Q. Xu, and Y. Cheng, "A compact and low-profile loop antenna with six resonant modes for LTE smartphone," *IEEE Transactions on Antennas and Propagation*, Vol. 64, No. 9, 3743–3751, 2016.

[4] Chen, H.-D., Y.-C. Tsai, C.-Y.-D. Sim, and C. Kuo, "Broadband eight-antenna array design for sub-6 GHz 5G NR bands metal-frame smartphone applications," *IEEE Antennas and Wireless Propagation Letters*, Vol. 19, No. 7, 1078–1082, 2020.

[5] Chang, L. and H. Wang, "Dual-band four-antenna module covering N78/N79 based on PIFA for 5G terminals," *IEEE Antennas and Wireless Propagation Letters*, Vol. 21, No. 1, 168–172, 2021.

[6] Wen, S., Y. Xu, and Y. Dong, "Low-profile wideband omnidirectional antenna for 4G/5G indoor base station application based on multiple resonances," *IEEE Antennas and Wireless Propagation Letters*, Vol. 20, No. 4, 488–492, 2021.

[7] Brandão, T. H. and A. Cerqueira, "Triband antenna array for FR1/FR2 5G NR base stations," *IEEE Antennas and Wireless Propagation Letters*, Vol. 22, No. 4, 764–768, 2022.

[8] Li, Y. and J. Chen, "Design of miniaturized high gain bowtie antenna," *IEEE Transactions on Antennas and Propagation*, Vol. 70, No. 1, 738–743, 2021.

[9] Rajanna, P. K. T., K. Rudramuni, and K. Kandasamy, "A high-gain circularly polarized antenna using zero-index metamate-rial," *IEEE Antennas and Wireless Propagation Letters*, Vol. 18, No. 6, 1129–1133, 2019.

[10] Ren, J., S. Gong, and W. Jiang, "Low-RCS monopolar patch antenna based on a dual-ring metamaterial absorber," *IEEE Antennas and Wireless Propagation Letters*, Vol. 17, No. 1, 102–105, 2017.

[11] Hui, W., Y. Guo, K. Xie, and X. Zhao, "Investigation of circularly polarized microstrip antenna with tri-band polarization conversion metamaterials," *IEEE Antennas and Wireless Propagation Letters*, Vol. 22, No. 12, 2831–2835, 2023.

[12] Hui, W., Y. Guo, and X. Zhao, "Polarization-tunable microstrip antenna based on double V-type metamaterials cover for microwave energy harvesting," *IEEE Antennas and Wireless Propagation Letters*, Vol. 22, No. 4, 729–733, 2022.

[13] Saghanezhad, S. A. H. and Z. Atlasbaf, "Miniaturized dual-band CPW-fed antennas loaded with U-shaped metamaterials," *IEEE Antennas and Wireless Propagation Letters*, Vol. 14, 658–661, 2014.

[14] Smith, D. R., D. C. Vier, T. Koschny, and C. M. Soukoulis, "Electromagnetic parameter retrieval from inhomogeneous metamaterials," *Physical Review E*, Vol. 71, No. 3, 036617, 2005.

[15] Wang, Z., Y. Ning, and Y. Dong, "Compact shared aperture quasi-Yagi antenna with pattern diversity for 5G-NR applications," *IEEE Transactions on Antennas and Propagation*, Vol. 69, No. 7, 4178–4183, 2020.

[16] Xu, Y., Y. Dong, S. Wen, and H. Wang, "Vertically polarized quasi-Yagi MIMO antenna for 5G N78 band application," *IEEE Access*, Vol. 9, 7836–7844, 2021.

[17] Huang, H., X. Li, and Y. Liu, "A low-profile, single-ended and dual-polarized patch antenna for 5G application," *IEEE Transactions on Antennas and Propagation*, Vol. 68, No. 5, 4048–4053, 2019.

[18] Jha, K. R., N. Rana, and S. K. Sharma, "Design of compact antenna array for MIMO implementation using characteristic mode analysis for 5G NR and Wi-Fi 6 applications," *IEEE Open Journal of Antennas and Propagation*, Vol. 4, 262–277, 2023.